

Synthesis and study of highly dense and smooth TiN thin films

Susmita Chowdhury, Rachana Gupta, Shashi Prakash

Applied Science Department, Institute of Engineering and Technology, DAVV, Indore, 452017.

Layanta Behera, D. M. Phase and Mukul Gupta*,

UGC-DAE Consortium for Scientific Research, University Campus, Khandwa Road, Indore 452 001, India

* *Corresponding author email: mgupta@csr.res.in*

Abstract

This study aims towards a systematic reciprocity of the tunable synthesis parameters - partial pressure of N_2 gas, ion energy (E_i) and Ti interface in TiN thin film samples deposited using ion beam sputtering at ambient temperature (300 K). At the optimum partial pressure of N_2 gas, samples were prepared with or without Ti interface at $E_i = 1.0$ or 0.5 keV. They were characterized using x-ray reflectivity (XRR) to deduce thickness, roughness and density. The roughness of TiN thin films was found to be below 1 nm, when deposited at the lower E_i of 0.5 keV and when interfaced with a layer of Ti. Under these conditions, the density of TiN sample reaches to $5.80(\pm 0.03)$ g cm^{-3} , a value highest hitherto for any TiN sample. X-ray diffraction and electrical resistivity measurements were performed. It was found that the cumulative effect of the reduction in E_i from 1.0 to 0.5 keV and the addition of Ti interface favors (111) oriented growth leading to dense and smooth TiN films and a substantial reduction in the electrical resistivity. The reduction in E_i has been attributed to the surface kinetics mechanism (simulated using SRIM) where the available energy of the sputtered species ($\langle E_{sp} \rangle$) leaving the target at $E_i = 0.5$ keV is the optimum value favoring the growth of defects free homogeneously distributed films. The electronic structure of samples was probed using N K-edge absorption spectroscopy and the information about the crystal field and spin-orbit splitting confirmed TiN phase formation. In essence, through this work, we demonstrate the role of $\langle E_{sp} \rangle$ and Ti interface in achieving highly dense and smooth TiN thin films with low resistivity without the need of a high temperature or substrate biasing during the thin film deposition process.

Keywords: transition metal nitrides, titanium nitride, ion beam sputtering, TiN film density

1. Introduction

Titanium nitride (TiN) films are well-known for several applications [1, 2, 3, 4, 5]. They are propitious refractory materials with their melting points exceeding 3000 K [1, 6] and in particular have been used as diffusion barriers [7], alternative plasmonic materials [8] in the visible and near-infrared (IR) regions at both high [9, 10] and low temperature [11]

regime and are well-known for providing superhardness (= 28 GPa) [12] due formation of strong covalent bonds between Ti and N atoms [13]. Thin films of TiN can be synthesized in a large compositional range within the NaCl type fcc structure and depending upon the composition, the density can vary in a rather large range [13]. Such variations in the ratio of Ti and N and the micro-structure leads to variable electrical resistivity of TiN films which typically

varies between 12.4 to 500 $\mu\Omega$ cm [14, 15].

Very recently, Zhang et al. [16] investigated TiN thin films interfaced with Ti using a direct current magnetron sputtering (dcMS) process together with an applied substrate bias of -70 V. Resulting films with (111) preferred orientation and low surface roughness showed the best performance for a synchronizer ring required in automobile industry. In addition, the utilization of TiN as an electrode in supercapacitors have accelerated the microelectronics technology in recent times [1]. Sun et al. [17] have showed that TiN films deposited at a substrate temperature (623 K) and substrate bias (-150 V dc) lowered the leakage current density by three order of magnitude compared to film deposited without substrate bias and demonstrated that denser film (density = 5.41 g cm⁻³) with $\sigma < 1$ nm and low resistivity ($\approx 31 \mu\Omega$ cm) plays a key role in the electrode performance. Additionally, the reduction in porosity of TiN films can also enhance the mechanical behavior [18, 19]. A study by Patsalas et al. [18] has revealed that both hardness and elastic modulus increases linearly with an increase in density of TiN films and the highest density achieved was 5.7 g cm⁻³ for TiN film (≈ 100 nm) deposited at a substrate temperature of 673 K and bias voltage of -100 V, though the nominal value of density of TiN film is expected to be about 5.4 g cm⁻³ [18]. However, due to large composition range and microstructure, the density of TiN films has been found to vary between 4.1 to 5.7 g cm⁻³ [18, 20]. Moreover, the tunability of film texturing (occurs due to lattice matched interface layers, substrates or high adatom mobility) [8, 21, 22] and compositional ratio (N/Ti atoms) can affect the hardness of the film [7, 12]. Several reports have confirmed that TiN films with (111) orientation comprises the highest hardness [23, 24, 25] and serves as a template for (111) oriented Al thin films, which reduces the electromigration of Al metal ions useful in microelectronics [26].

Here, it is to be noted that the addition of Ti (0002) as an interface escalates the (111) texturing of TiN films due to the coherent atomic matching $\approx 98.4\%$ of both planes [27] and has been a topic of research for several decades. An alternate approach of such (111) texturing was demonstrated by Lattemann et al. [28]

utilizing high power impulse magnetron sputtering (HiPIMS), where the high-flux ionization species assisted the (111) grain growth even at room temperature with dense micro-structure. However, the dense morphology was confirmed by HRTEM measurements but the density of those TiN films (≈ 100 nm) was not measured. Further, the HiPIMS process suffers from low deposition rates. Hence, it is clear that (111) textured films with improved microstructural morphology (denser and smoother surface) is a prerequisite from application based perspectives and few attempts that were made are listed in Table 1.

Forepart, among the extensive adopted deposition techniques, relatively less attention has been dedicated for the synthesis of TiN thin films under ambient conditions i.e. without substrate bias and heating [29, 30, 28, 31, 32]. Deposition of dense TiN films under ambient conditions is not only cost effective, it also reduces the diffusion probability with the substrate or with other layers in a multilayers stack. The opted room-temperature deposition techniques were HiPIMS, dcMS or dual ion beam sputtering (DIBS) etc. where the sputtering powers, substrate temperatures, acceleration voltages, film thicknesses were modulated and even incorporation of Ti interface was done to detect the inter-dependence of the process parameters on the film growth and microstructures. On the contrary in this work, we used a simpler IBS process without any substrate heating or bias to deposit TiN thin films. The partial pressure of N₂ gas was precisely controlled using a ultra-high vacuum (UHV) leak valve in the vicinity of the substrates. The incident ion energy (E_i), was varied which in turn varies the energy of the sputtered species $\langle E_{sp} \rangle$ leaving the target. Since, $\langle E_{sp} \rangle$ is known to affect the thin film growth, its implication on the growth of TiN films deposited without or with Ti interface was studied. The self-hood of the work reclines in successful growth of denser and smoother TiN films by reducing the E_i from 1 to 0.5 keV when interfaced with Ti, having the highest density of TiN thin film hitherto.

Table 1: A literature survey of TiN thin films deposited using different deposition methods and various process parameters without or with Ti interface. Here, dcMS = direct current magnetron sputtering, rfMS = radio frequency magnetron sputtering, HiPIMS = High power impulse magnetron sputtering, IBAD = ion beam assisted deposition, DIBS = dual ion beam sputtering, IBS = ion beam sputtering, T_s = substrate temperature, V_b = substrate bias voltage, Ti = Titanium interface layer, σ = surface roughness, ρ_{el} = electrical resistivity.

Deposition Method	Process Parameters	Density (g cm^{-3})	σ (nm)	ρ_{el} ($\mu\Omega \text{ cm}$)	Reference
dcMS	$V_b = -150 \text{ V}, T_s = 623 \text{ K}$	5.41	< 1	31	[17]
dcMS	$V_b = 0 \text{ V}, T_s = 623 \text{ K}$	4.77	1.9	105.2	[17]
dcMS	$V_b = -100 \text{ V}, T_s = 673 \text{ K}$	5.7	–	–	[18]
dcMS	$V_b > -100 \text{ V}; T_s = 923 \text{ K}$	5.7	–	40	[33]
rfMS	$V_b = 0 \text{ V}, T_s = 873 \text{ K}$	4.14	–	70.2	[20]
HiPIMS	$V_b = 0 \text{ V}, T_s = 300 \text{ K}$	5.30	–	130	[31]
IBAD	$V_b = 0 \text{ V}, T_s = 300 \text{ K}$	–	–	400	[15]
DIBS	$V_b = 0 \text{ V}, T_s = 300 \text{ K}$	5.2 - 5.3	< 1	–	[30]
dcMS	Ti, $V_b = -70 \text{ V}, T_s < 423 \text{ K}$	–	> 7.8	–	[16]
dcMS	Ti, $V_b = 0 \text{ V}, T_s = 723 \text{ K}$	–	3.3	–	[34]
IBS	$V_b = 0 \text{ V}, T_s = 300 \text{ K}$	5.79	0.7	117	this work
IBS	Ti, $V_b = 0 \text{ V}, T_s = 300 \text{ K}$	5.80	0.6	91	this work

2. Methodology

A series of TiN thin films without and with a Ti interface were deposited on a single crystal Si (100), amorphous glass and quartz substrates at room temperature (300 K, no intentional heating). Substrates were thoroughly cleaned in an ultrasonic bath prior to the deposition. Samples were deposited using a home-made radio frequency Ion Beam Sputtering (rf-IBS) system [35]. A Veeco 3 cm rf (13.56 MHz) ion source was used to ionize 5N purity Ar gas flowing at 5 sccm and a similar amount of Ar gas was also used to neutralize the ion beam. The Ar ion beam was kept incident at an angle of about 45° to sputter Ti target (purity 99.99%). A schematic diagram of the rf-IBS system is shown in the Supplementary Material (SM) [36]. Prior to the deposition, the base pressure achieved in the chamber was about 1×10^{-7} Torr or lower. To achieve nitridation of adatoms, N_2 gas was flown in the chamber in the vicinity of substrates using an ultra-high vacuum (UHV) leak valve. The N_2 partial pressure (P_{N_2}) was raised from 1×10^{-7} Torr to 2.5, 5.0 and 7.5×10^{-5} Torr. Incident Ar ion energy E_i was kept either at 1.0 or at 0.5 keV. Details of samples and deposition conditions are given in table 2.

Table 2: Details of samples and deposition parameters used during deposition. Here, P_{N_2} is the nitrogen partial pressure and E_i is the incident energy of the Ar^+ ions.

Sample code	Sample details	P_{N_2} ($\times 10^{-5}$ Torr)	E_i (keV)
Ti	Ti (10 nm)	0.0	1.0
TiN-1	TiN (100 nm)	2.5	1.0
TiN-2	TiN (100 nm)	5.0	1.0
TiN-3	TiN (100 nm)	7.5	1.0
TiN-4	TiN (100 nm)	2.5	0.5
TiN-5	Ti(10 nm)/TiN(90 nm)	2.5	1.0
TiN-6	Ti(10 nm)/TiN(90 nm)	2.5	0.5

The long-range structural ordering was characterized by x-ray diffraction (XRD) using Bruker D8 Advance XRD system based on θ - 2θ Bragg-Brentano geometry. The Cu-K α source produced x-rays of wavelength 1.54 Å and they were detected using a fast 1D detector (Bruker LynxEye). The density, thickness and roughness of the as-deposited samples were analyzed using x-ray reflectivity (XRR) measurements performed on a Bruker D8 Discover system using Cu-K α x-rays. To probe the surface morphology at the atomic scale level, atomic force microscopy (AFM) measurements were done in non-contact mode over a scan area of $2 \times 2 \mu\text{m}^2$ (can be seen in SM) [36]. The dc electrical resistivity ρ_{el} of the samples were performed by collinear standard four-probe method at room temperature keeping the current fixed at $\pm 105 \mu\text{A}$. Surface sensitive soft x-ray absorption near edge spectroscopy (SXAS) measurements were carried out at BL-01 [37] beamline at Indus-2 synchrotron radiation source at RRCAT, Indore, India. The synchrotron radiation source was operating at an electron energy of 2.5 GeV and a beam current of 150 mA. SXAS measurements were performed at N K-edge and Ti L $_{3,2}$ edges in total electron yield (TEY) mode which allows to collect all the electrons ejected out from the sample surface probing a depth of about 10 nm [38]. A computational analysis of $\langle E_{\text{sp}} \rangle$ was performed by stopping and range of ions in matter (SRIM) [39]. The analysis was performed for a sampling of 10^5Ar^+ ions impinging on the target surface with an angle of inclination of 45° , similar to the experimental condition used in this work.

3. Results and discussion

3.1. X-ray reflectivity

The XRR pattern of TiN thin films prepared using different values of P_{N_2} at 1 keV (TiN-1, TiN-2 and TiN-3) are shown in Fig. 1 as a function of momentum transfer vector (q_z). They were fitted using Parratt 32 software [40] based on Parratt's formalism [41]. The inset of Fig. 1 compares XRR data of these samples depicting small changes in the critical q_z (taken approximately at 50% intensity) given by $q_c = 4\pi \sin\theta_c/\lambda$, where $\theta_c = \sqrt{2\delta} = \sqrt{\lambda^2 \rho/\pi}$ is the

critical angle, δ is dispersive part of the refractive index of the material, ρ is scattering length density (SLD) of the material and λ is the wave-length of x-rays [42]. With the known values of ρ obtained from the fitting of XRR data, mass density (ρ_{m}) of samples were obtained (assuming TiN stoichiometry). The fitting step includes a thin ($< 3 \text{nm}$) titanium oxynitride layer (TiO_xN_y) on TiN thin films followed by an interface layer ($< 2 \text{nm}$) of some titanium oxide (Ti_xO_y) on Si substrates. It is known that TiN films are affected by surface oxidation to a large extent on exposure to atmosphere due to higher affinity of Ti towards oxygen (ΔH_f^0 ranging between -542 to -1521 kJ mol $^{-1}$ for different compositions of Ti_xO_y at 298K). However, in our TiN thin films the SLD of the topmost oxide layer comes out to be higher than the known forms of Ti_xO_y indicating the presence of some TiO_xN_y . Here it is worth mentioning that with increase in P_{N_2} , the contribution of surface oxidation gradually reduces, as expected. Moreover, even the presence of negligible amount of O_2 in the deposition chamber can also form oxide layer in the substrate-film interface which was also evidenced in our samples. The O_2 base pressure was $\approx 7.5 \times 10^{-10}$ Torr in our chamber (measured using a residual gas analyzer) [43], and it seems that this negligible amount of O_2 readily reacts with Ti forming a thin ($< 2 \text{nm}$) Ti_2O_3 phase during the early stage of growth ($\Delta H_f^0 = -1521 \text{kJ mol}^{-1}$ for Ti_2O_3 compared to -337kJ mol^{-1} for TiN). Detailed fitted parameters are listed in Table 3.

The deposition rate (DR) using pure Ar was 40.2 Å/min for Ti, and decreases to 21.9, 17.8, and 16.1 Å/min in TiN-1, TiN-2 and TiN-3 samples. A reduction in DR can be associated to the nitridation of the target itself known as target poisoning [44, 45, 46]. Generally, DR from a fully poisoned target become negligibly small [47, 48]. In the present case, the TiN-3 sample ($P_{\text{N}_2} = 7.5 \times 10^{-5}$ Torr) seems to be at the onset of target poisoning but the formation of a TiN phase in TiN-1 and TiN-2 samples is taking place from a so called transient state lying somewhere between the metallic and poisoned state [48]. Such a reduction in DR can be attributed to the formation of much stronger chemical bonds

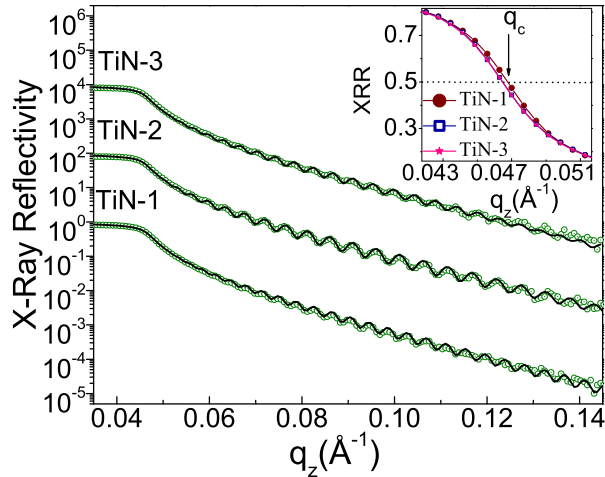


Figure 1: X-ray reflectivity pattern of TiN samples deposited at various P_{N_2} of 2.5×10^{-5} (TiN-1), 5×10^{-5} (TiN-2) and 7.5×10^{-5} Torr (TiN-3). The patterns are shifted along the y-axis for clarity. The inset compares the variation in the vicinity of critical angle region. Here, the open circles represent the experimental data and solid lines show the theoretical fitting.

of the compound on the target surface (with the introduction of N_2 flow) than the elemental metallic bonds present within the target resulting in lowering of DR [46]. Subsequently, the SLD also reduces as can be seen from Table 3 yielding reduction in ρ_m from 5.42 (TiN-1) to 5.36 (TiN-2) and to 5.33 g cm^{-3} (TiN-3). From the observed values, it can be seen that the density of the sample labelled as TiN-1 appears to be in the closest agreement with that of stoichiometric bulk TiN ($\approx 5.4 \text{ g cm}^{-3}$) [18]. Within the present experimental conditions (using a UHV leak valve), the minimum control level of P_{N_2} was about 5×10^{-6} Torr and already at a low partial gas flow of 2.5×10^{-5} Torr, stoichiometric TiN is achieved. When flow is increased further (which was also evidenced by the residual gas analyzer), it apparently creates voids or disorder leading to a reduction in the density of the films. This becomes clearer after comparing the XRD results presented in section 3.2.

Table 3: Parameters of TiN thin films obtained from of x-ray reflectivity (XRR) measurements. Here, scattering length density (SLD) and rms surface roughness (σ) was obtained from fitting of XRR data.

Sample code	SLD (± 0.02 $\times 10^{-5} \text{ \AA}^{-2}$)	σ ($\pm 0.2 \text{ nm}$)
TiN-1	4.35	1.4
TiN-2	4.30	1.3
TiN-3	4.28	1.4
TiN-4	4.65	0.9
TiN-5	4.60	0.9
TiN-6	4.66	0.9

3.2. X-ray diffraction

Fig. 2 shows the XRD patterns of TiN-1, TiN-2 and TiN-3 samples. In case of TiN-1 sample, prominent peaks occurring at $2\theta = 36.08$ and 42.05° can be assigned to TiN (111) and TiN (200) reflections [49]. With increasing P_{N_2} , the peak corresponding to (111) lattice plane shifts towards lower 2θ whereas the (200) peak slightly displaces towards the higher angle region (depicted more clearly in the inset of Fig. 2 for TiN-1, TiN-2 and TiN-3 samples). However, both these reflections become broadened due to lack of crystalline long range ordering with increasing P_{N_2} . Detailed values of lattice parameters (LP) obtained from both lattice planes and the crystallite size (D) obtained from the most intense (111) peak using Scherrer's formula are given in SM [36]. For TiN-1, the deduced LP are $a^{111} = 4.30 (\pm 0.01) \text{ \AA}$ and $a^{200} = 4.29 (\pm 0.01) \text{ \AA}$. Similar values (within the experimental accuracy) of LP obtained from both the (111) and (200) lattice planes are expected in a cubic symmetry. Comparing the value of LP in our samples, it is evident that the samples exhibit in-plane compressive stress common in room temperature deposited ion beam sputtering techniques [30] but lies within the experimental values obtained in different works [18, 50, 51, 52]. Generally, the LP of TiN has been found anywhere between 4.18 - 4.40 \AA [50, 51, 53], where in a number of works the LP of 4.30 \AA has also been obtained and assigned to be in δ -TiN phase [18, 50, 51, 52]. Therefore, it can be concluded that our TiN-1 sample is closest to sto-

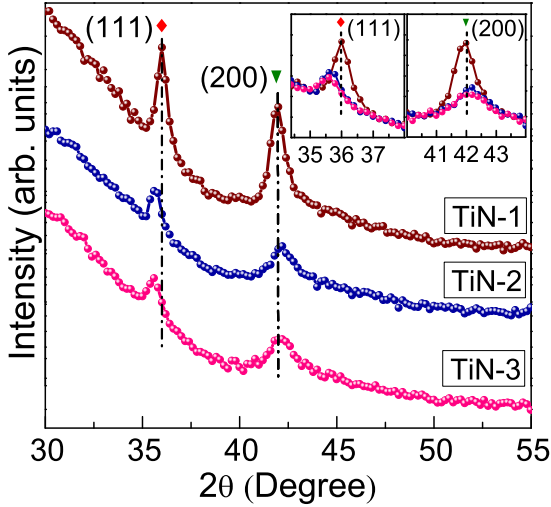


Figure 2: X-ray diffraction pattern of TiN samples deposited at ambient temperature (300K) for different P_{N_2} of 2.5×10^{-5} (TiN-1), 5×10^{-5} (TiN-2) and 7.5×10^{-5} Torr (TiN-3). The inset compares the peak positions around (111) and (200) peaks.

ichiometric δ -TiN, which is also supported by XRR results.

By increasing the P_{N_2} , we find that LP obtained from the (111) reflection increases whereas that of (200) decreases. This indicates some distortion from the cubic symmetry [54]. As we find from our XRR results also, the density of film decreases in TiN-2 and TiN-3 samples. It appears that over-saturation of nitrogen in TiN may lead to such effects.

3.3. Influence of ion energy on growth behavior of TiN thin films

From the results shown in section 3.1 and 3.2 (XRR and XRD results), we found that nearly stoichiometric TiN phase was obtained in TiN-1 sample. Therefore, keeping the parameters similar as in TiN-1, a sample was grown by reducing E_i to 0.5 keV and labelled as TiN-4. A comparison of XRR and XRD data of TiN-1 and TiN-4 samples are shown in Fig. 3. The fitting of XRR pattern of TiN-4 sample was also performed following a similar procedure as mentioned

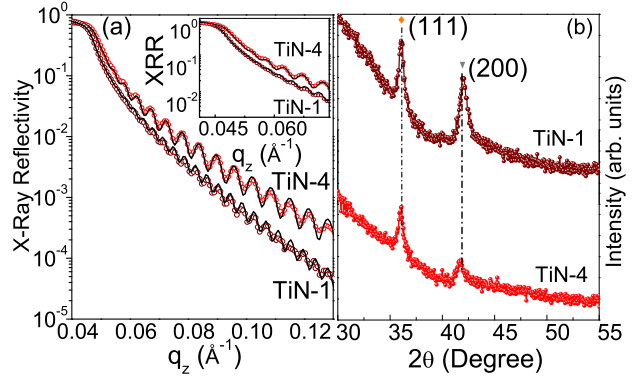


Figure 3: XRR (a) and XRD (b) patterns of TiN-1 and TiN-4 thin films deposited at variable incident ion energies of 1 and 0.5 keV with a constant Ar gas flow of 5 sccm and P_{N_2} of 2.5×10^{-5} Torr. The inset of (a) compares the critical density region of TiN-1 and TiN-4 thin films. Here, the open circles represent the experimental data and solid lines show the theoretical fitting in (a).

in section 3.1. Here the data of TiN-1 sample is the same as presented in Fig. 1 and 2. The effect of reduction of E_i on the XRR pattern can be seen in terms of a less steeper decay of XRR pattern. It is known that XRR pattern is affected by the rms roughness (σ) of the sample surface as, $R \propto e^{-q_z^2 \sigma^2}$ where R is the specular reflectivity from the sample surface [55]. Therefore, it becomes clear that the roughness of the sample deposited at lower E_i is smaller. In addition, the SLD of this sample also comes out to be higher (this becomes evident by comparing the q_c region as shown in the inset of Fig. 3 (a) yielding $\rho_m = 5.79 \text{ g cm}^{-3}$). Fitted parameters of TiN-4 sample are also shown in Table 3. It is somewhat surprising to note that the density of TiN-4 sample at 5.79 g cm^{-3} surpasses the previous highest value of 5.7 g cm^{-3} achieved by Patsalas et al. [18] in TiN thin film samples grown at a very high substrate temperature (673 K) together with an applied bias voltage of -100 V. In contrast, our sample was grown at room temperature (300 K) without any substrate biasing. From the fitting parameters as shown in Table 3, we can see that roughness ($\approx 0.9 \text{ nm}$) of the film reduces to sub-nanometer region in spite of the fact that the

film thickness being fairly large at about 90 nm.

The effect of reduced E_i on the XRD pattern is shown in Fig. 3 (b). In comparison to the TiN-1 sample, we can see that the peak positions in this sample (TiN-4) are also similar resulting in similar value of LP [36]. On the other hand, the significant difference between TiN-1 and TiN-4 samples can be seen in terms of relative intensities of (111) and (200) reflections as can be observed from the XRD fitting. In case of TiN-1, $I_{(111)} = 0.57 I_{(200)}$ signifying that (200) reflection is more pronounced compared to (111), where $I_{(hkl)}$ signifies the area under the curve for the particular (hkl) reflection whereas for TiN-4, $I_{(111)} = 1.79 I_{(200)}$ clearly stating that texturing of (111) reflection is favored in the later case. Moreover, the prominent effect in the reduction of E_i can be manifested in terms of reduced roughness and increasing density and it can be correlated to $\langle E_{sp} \rangle$ of the sputtered species leaving the target which in turn modifies the growth kinetics by changing the adatom diffusion lengths during the film growth. To evaluate $\langle E_{sp} \rangle$, SRIM simulations were performed on Ti targets in pure Ar environment and the effect of surface binding energy was also taken into account to obtain the correct values [39, 56]. For $E_i = 1$ keV and 0.5 keV, the calculated values of $\langle E_{sp} \rangle$ (eV/atom) are 35.2 ± 2 and 27.1 ± 2 , respectively which can be suitably translated to TiN. The effect of such influence on $\langle E_{sp} \rangle$ ($\approx 20\%$ reduction by changing E_i from 1 to 0.5 keV) is in particularly significant for TiN whereas other elements (e.g. nickel) does not seem to be affected so much by such an incremental change in E_i . This was amply demonstrated on surfactant mediated growth of Ti/Ni multilayers [57]. The consequence of variation in adatom mobility is enhanced (200) reflection occupying the lowest surface energy site in TiN-1, albeit in TiN-4 the preferred orientation is reversed (along (111) plane) favoring the closely packed plane by lowering the overall energy of the crystal which is expected in kinetics driven mechanism [18].

In essence, the effect of reduction in the E_i has positively influenced the growth of TiN film which has a very dense microstructure as well as low roughness. However, since the $I_{(200)}$ has not been completely suppressed, we utilized a Ti interface both at $E_i = 1.0$ and 0.5 keV in the next section 3.4.

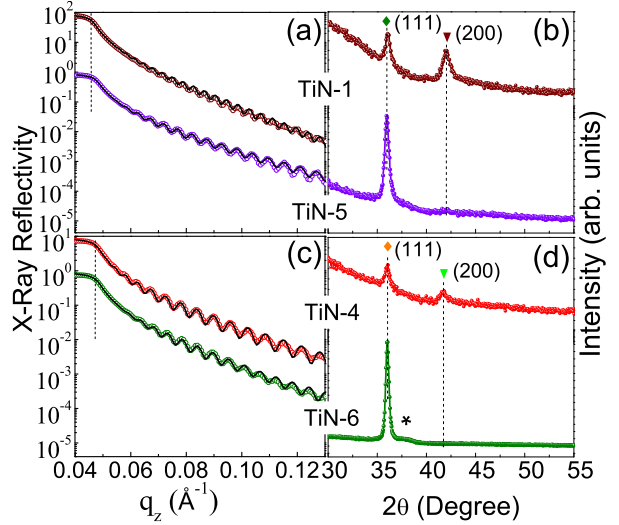


Figure 4: The XRR (a) and XRD (b) data of TiN-1 and TiN-5 samples deposited at an ion energy of 1 keV with same Ar gas flow pf 5 sccm and P_{N_2} of 2.5×10^{-5} Torr. A comparison of XRR (c) and XRD (d) patterns are shown at a reduced ion energy of 0.5 keV for TiN-4 and TiN-6 thin films deposited at same deposition parameters. Here, the open circles represent the experimental data and solid lines show the theoretical fitting in (a) and (c).

3.4. Effect of Ti interface on texturing of TiN thin films

Fig. 4 (a) and 4 (b) compares the XRR and XRD data of samples prepared without (TiN-1) and with Ti interface (TiN-5) deposited under similar conditions (P_{N_2} of 2.5×10^{-5} Torr, $E_i = 1.0$ keV) whereas Fig. 4 (c) and 4 (d) compare the samples deposited without (TiN-4) and with Ti interface (TiN-6) deposited at reduced $E_i = 0.5$ keV keeping P_{N_2} unaltered. As mentioned earlier in section 3.1 and 3.3, a thin layer of TiO_xN_y phase was introduced for TiN-5 and TiN-6 samples as well, corresponding to surface oxidation. The same intermediate phase of Ti_xO_y (< 2 nm) was also introduced between Ti and Si surface for TiN-5 and TiN-6 samples. The fitted parameters are shown in table 3. The ρ_m values obtained from SLD which was ini-

tially 5.42 g cm^{-3} for TiN-1 film increased to 5.73 g cm^{-3} for TiN-5 sample with the introduction of Ti interface. This is expected because the close packed hexagonal structure of Ti interface promotes growth of smoother and denser TiN films with a low surface roughness of 0.9 nm . Moreover, mixed orientations found in TiN-1 sample get completely diminished and texturing of (111) plane was achieved with a small trace of (200) reflection in the presence of thin (10 nm) Ti interface for TiN-5 film (90 nm) as shown in Fig. 4 (b). It is well known that such unidirectional grain growth occurs due to the coherent atomic matching ($\approx 98.4\%$) of the (0002) Ti plane with the (111) plane of TiN leading to minimization of the interfacial strain [21, 34]. Additionally, Ti interface provides better adhesion between film and the substrate by reducing the residual stress [58].

Similar trends in XRR and XRD were also observed for TiN-4 and TiN-6 samples (as shown in Fig. 4 (c) and 4 (d)). The ρ_m of TiN-6 film comes out to be 5.8 g cm^{-3} , even larger than that of TiN-4 sample and the roughness remains low at 0.9 nm in both samples. From the XRD pattern as shown in Fig. 4 (d), the presence of Ti phase (the broad feature shown by an asterisk (*)) was detected accompanied with a highly textured (111) orientation of the TiN-6 film. In addition, the (200) plane was completely suppressed for TiN-6 films in comparison to TiN-4. Hence, from the above results it is evident that kinetics of lowering in adatom mobility (due to variation of $\langle E_{sp} \rangle$ as obtained from SRIM calculation) consequences in preferred orientation of densely packed (111) plane with relatively smaller grain size (as can be seen from SM [36]) which reduces defects (in the form of voids) in the crystal lattice and results in densification as seen for TiN-4 thin films and the addition of Ti interface results in texturing of the TiN-6 film with dense microstructure. Moreover, increase in density of TiN-6 films with addition of densely packed Ti interface is less pronounced in the present case as the film was already voids free during low ion energy deposition (as for TiN-4) but it promoted larger grain growth of the TiN-6 sample.

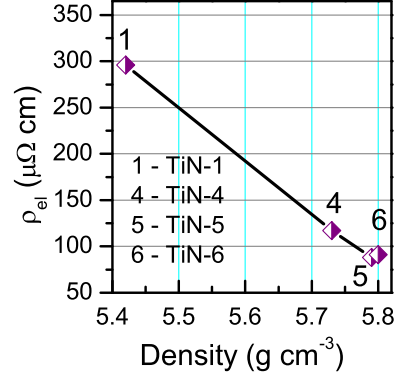


Figure 5: The variation in the electrical resistivity (ρ_{el}) of TiN thin film samples deposited at $E_i = 1.0$ (TiN-1 and TiN-5) and 0.5 keV (TiN-4 and TiN-6) without (TiN-1 and TiN-4) and with (TiN-5 and TiN-6) Ti interface at a constant Ar gas flow of 5 sccm and $P_{N_2} = 2.5 \times 10^{-5} \text{ Torr}$.

3.5. Room-temperature resistivity

Furthermore, to get an insight on the electrical transport behavior, the resistivity (ρ_{el}) measurements were performed at room-temperature. The variation of ρ_{el} with the density of different TiN thin film samples is shown in Fig. 5. As can be seen from this figure that ρ_{el} decreases almost linearly moving from sample TiN-1 to TiN-4 to TiN-5/TiN-6. This implies that the reduction of E_i from 1 to 0.5 keV or the introduction of Ti interface or both lead to denser films with lower values of ρ_{el} . Here, it is worth mentioning that the ρ_{el} of TiN typically lies between 30 to $450 \mu\Omega \text{ cm}$ [15, 29] but application of substrate bias, substrate temperature etc. substantially reduces the ρ_{el} values due to annihilation of the defects and structural relaxation at relatively higher energy [15, 20]. For room temperature deposited TiN films, Yang et al. reported a value of $130 \mu\Omega \text{ cm}$ using HiPIMS [31]. In contrast, $\rho_{el} = 400 \mu\Omega \text{ cm}$ was obtained by Yokota et al. in IBAD [15] deposited TiN thin films. And even $\rho_{el} > 500 \mu\Omega \text{ cm}$ was reported by Kearney et al. [20] using rfMS. Fig. 5 depicts an inverse relation between the ρ_{el} and density of the samples, which is a general trend that is indeed expected [29]. Subsequent to the fact that all the samples typically exhibit the same thickness ($90 - 100 \text{ nm}$) and have been

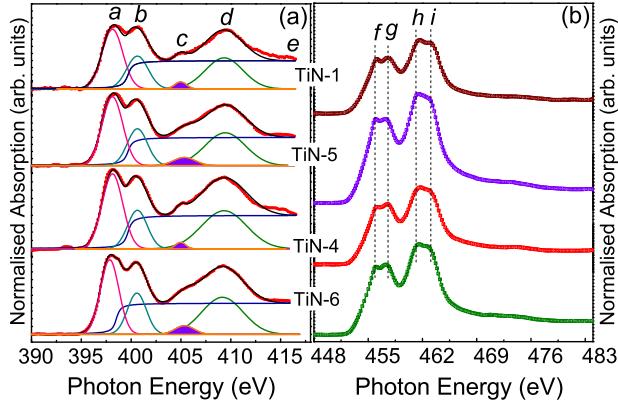


Figure 6: Normalised SXAS spectra of fitted N K-edge (a) and Ti L-edge (b) of TiN thin films deposited without and with Ti interface at variable incident ion energies of 1 and 0.5 keV at a constant Ar gas flow of 5 sccm and $P_{N_2} = 2.5 \times 10^{-5}$ Torr. Here, the open circles represent the experimental data and solid lines show the theoretical fitting in (a).

deposited at same temperature (300 K), such a variation can be attributed to the suppression of the defects across the film surface and the grain boundary sites due to significant reduction in $\langle E_{sp} \rangle$ and addition of Ti interface, which in-turn leads to larger grain growth and considerable reduction in porosity of the films. It yields lowering in scattering of the conduction electrons with the defects, which plays a dominant role at ambient temperature [59, 60]. The result is in accordance with the XRD data as well, where an inverse proportionality between the crystallite size and the resistivity of the samples can be observed (see SM) [36].

3.6. Soft X-ray Absorption Spectroscopy

Fig. 6 (a) compares the normalised and fitted N K-edge spectra whereas Fig. 6 (b) shows the Ti $L_{3,2}$ features of TiN-1, TiN-4 ($E_i = 1$ keV) and TiN-5, TiN-6 ($E_i = 0.5$ keV) samples deposited without and with Ti interface. It is well known that intensity of XAS spectra probe the unoccupied density of states making it an element specific technique. The pre and post edge normalisation as well as the fitting of N K-edge spec-

tra were processed through ATHENA software based on the numerical algorithms of IFEFFIT library [61]. Fig. 6 (a) shows the fitted N K-edge XAS spectra and the fitting involves an arc tangent step function followed by four Gaussian envelopes corresponding to the features ‘a’, ‘b’, ‘c’, ‘d’ and detailed peak positions are listed in SM [36]. The N K-edge features of TiN samples reveal that the doublet marked as ‘a’ and ‘b’ near the threshold appears due to the unoccupied hybridized molecular orbitals of TiN i.e. t_{2g} (Ti 3d states overlapped with N $2p\pi$) and e_g (Ti 3d states mixed with N $2p\sigma$) orbitals, respectively. Such sharp intense peaks (‘a’ and ‘b’) are characteristic features of cubic rocksalt structure of TiN [62]. The shoulder ‘c’ and broad feature ‘d’ in the higher energy range are depicted as the excitation to Ti 4sp hybridized with N 2p states. Feature ‘e’ is due to intermixing of higher energy unoccupied orbitals such as Ti 4p + N 2p-3p states [63]. The octahedral crystal field splitting $10Dq$ ($E_b - E_a$) for TiN-1, TiN-5 and TiN-4 are found to be ≈ 2.5 (± 0.1) eV whereas for TiN-6 sample it comes out to be ≈ 2.6 (± 0.1) eV, which matches well with the generally observed value of 2.5 eV [64, 65]. Further proceeding towards the higher energy regime reveal that for samples TiN-1 and TiN-4, the feature ‘c’ are alike having steeper slopes in comparison to TiN-5 and TiN-6 samples. Such smooth variation of feature ‘c’ have been witnessed for strong (111) texture of TiN films [51, 66]. The variations can be attributed to the long range ordering sensitivity of feature ‘c’ due to higher scattering effects [65] and hence it is obvious that highly close packed (111) textured films can suppress such contribution.

To get an idea about the spin-orbit coupling, the Ti L-edge features were also studied. Here, it is worth mentioning that Ti L-edge consists of two features (L_3 and L_2) which arises due to the transition of core electron from Ti $2p_{3/2} \rightarrow Ti 3d$ and Ti $2p_{1/2} \rightarrow Ti 3d$ respectively [67]. Although, our obtained Ti L-edge features are not consistent with the literature reports [67, 68] and clearly confirms the presence of surface oxidation which was in accordance with our XRR fitting. From Fig. 6 (b) the four features marked as ‘f’ (Ti $2p_{3/2} \rightarrow O2p\pi + Ti3d$), ‘g’ (Ti $2p_{3/2} \rightarrow O2p\sigma + Ti3d$), ‘h’ (Ti $2p_{1/2} \rightarrow O2p\pi + Ti3d$)

and ‘*i*’ (Ti 2p_{1/2}→O2pσ+Ti3d) can be assigned to L₃-t_{2g}, L₃-e_g, L₂-t_{2g} and L₂-e_g transitions which arise due to the octahedral crystal field splitting [38]. But surprisingly the 2p spin-orbit coupling in all samples are found to be ≈ 5.5 eV which is in well agreement with that of surface oxidation free TiN films where a capping layer of Al was used to avoid surface contaminations [67]. However, spectral modifications is quite often in Ti L-edge spectra due to the multiplet effect which plays a dominant role for early transition metal nitride films like TiN [38]. In essence, the Ti L-edge measurements are in agreement with other measurement (e.g. XRR) and the N K-edge spectra of TiN-5 and TiN-6 samples clearly confirms the dominant (111) orientation as considered from XRD measurements.

4. Conclusion

In conclusion, the role of probing variable ion energy without and with Ti interface on the resulting growth behavior of TiN thin films with film microstructure, electrical behavior and electronic nature has been studied systematically in details. The study reveals that reduction in the ion energy results in denser and smoother films with appreciable reduction in the electrical resistivity, favoring the closely packed (111) preferred orientation which can be interpreted in terms of surface kinetics of adatom mobility pronounced for TiN thin films as calculated from SRIM. The $\langle E_{sp} \rangle$ which was initially ≈ 35 eV/atom at $E_i = 1$ keV reduced to ≈ 27 eV/atom for $E_i = 0.5$ keV. Moreover, introduction of room temperature deposited Ti interface with 10 nm thickness serves as a template for (111) texturing (also confirmed from our SXAS data) of the films resulting in dense microstructure. Hence, it leads to a mass density of 5.8 g cm⁻³ for TiN sample deposited at $E_i = 0.5$ keV with Ti interface at room temperature. It is worth mentioning that this is the highest obtained density so far in TiN thin films to the best of our knowledge and the reproducibility of the data was ensured several times through XRR measurements. In addition, these samples show substantially low resistivity (≈ 90 μΩ cm) value, which is among the lowest obtained values for room temperature deposited TiN

films. Thus, it can be anticipated that IBS technique is one of the preferred techniques where the appreciable modulation in $\langle E_{sp} \rangle$ is especially effective for Ti interfaced TiN thin films which can enhance the surface morphology of the resulting ultra-dense crystal lattice with surface roughness down to subnanometer (< 1 nm) regime and lowest resistivity values even at room temperature. Hence, our findings depict pathways for enhanced surface morphology with low electrical transport response of TiN thin films (at room temperature with no intentional substrate bias or substrate heating) to an extent to avoid interfacial diffusion probability of TiN thin films common in thin film synthesis, usage in microelectronics and many more.

Acknowledgments

Authors (SC and RG) are grateful to UGC-DAE CSR, Indore for providing financial support through CSR-IC-BL-62/CSR179-2016-17/843 project. Thanks are due to V. R. Reddy and Anil Gome for XRR measurements, Rajeev Rawat and Dileep Kumar for the resistivity measurements, R. Venkatesh and Mohan Gangrade for AFM measurements, Rakesh Sah and Avinash Wadikar for SXAS measurement at BL-01, Indus 2, RRCAT, Indore, India. We also thank S. Tokekar, A. K. Sinha, A. Banerjee and V. Ganesan for their kind support and constant encouragements. SC is thankful to Yogesh and Shailesh for the help provided in depositions.

References

- [1] J. Shi, B. Jiang, C. Li, F. Yan, D. Wang, C. Yang, J. Wan, Review of transition metal nitrides and transition metal nitrides/carbon nanocomposites for supercapacitor electrodes, *Materials Chemistry and Physics* 245 (2020) 122533.
- [2] M. Golebiewski, G. Kruzal, R. Major, W. Mróz, T. Wierzchoń, R. Ebner, B. Major, Morphology of titanium nitride produced using glow discharge nitriding, laser remelting and pulsed laser

- deposition, *Materials Chemistry and Physics* 81 (2003) 315 – 318.
- [3] N. Arshi, J. Lu, Y. K. Joo, C. G. Lee, J. H. Yoon, F. Ahmed, Study on structural, morphological and electrical properties of sputtered titanium nitride films under different argon gas flow, *Materials Chemistry and Physics* 134 (2012) 839 – 844.
- [4] M. Kiuchi, A. Chayahara, M. Tarutani, Y. Takai, R. Shimizu, The microstructure of transparent and electrically conducting titanium nitride films, *Materials Chemistry and Physics* 54 (1998) 330 – 333. URL:
- [5] M. Raaif, Investigating the structure and tribomechanical performance of pvd tin on bearing tin substrate constructed by rf plasma, *Materials Chemistry and Physics* 224 (2019) 117 – 123.
- [6] L. E. Toth, *Refractory materials, Transition Metal Carbides and Nitrides*, Academic Press Inc., New York 7 (1971) 88.
- [7] J. H. Huang, C. H. Ma, H. Chen, Effect of Ti interlayer on the residual stress and texture development of TiN thin films, *Surface and Coatings Technology* 200 (2006) 5937–5945.
- [8] P. Patsalas, N. Kalfagiannis, S. Kassavetis, G. Abadias, D. Bellas, C. Lekka, E. Lidorikis, *Conductive nitrides: Growth principles, optical and electronic properties, and their perspectives in photonics and plasmonics*, *Materials Science and Engineering: R: Reports* 123 (2018) 1–55.
- [9] G. V. Naik, J. L. Schroeder, X. Ni, A. V. Kildishev, T. D. Sands, A. Boltasseva, Titanium nitride as a plasmonic material for visible and near-infrared wavelengths, *Optical Materials Express* 2 (2012) 478–489.
- [10] A. Boltasseva, Empowering plasmonics and metamaterials technology with new material platforms, *MRS Bulletin* 39 (2014) 461–468.
- [11] L. Vertchenko, L. Leandro, E. Shkondin, O. Takayama, I. V. Bondarev, N. Akopian, A. V. Lavrinenko, Cryogenic characterization of titanium nitride thin films, *Optical Materials Express* 9 (2019) 2117–2127.
- [12] W. L. Pan, G. P. Yu, J. H. Huang, Mechanical properties of ion-plated TiN films on AISI D2 steel, *Surface and Coatings Technology* 110 (1998) 111–119.
- [13] J. E. Sundgren, B. Johansson, A. Rockett, S. Barnett, J. Greene, $\text{TiN}_x(0.6 < x < 1.2)$: Atomic arrangements, Electronic structure and recent results on crystal growth and physical properties of epitaxial layers, in: *AIP Conference Proceedings*, volume 149, 1986, pp. 95–115.
- [14] B. W. Karr, D. G. Cahill, I. Petrov, J. Greene, Effects of high-flux low-energy ion bombardment on the low-temperature growth morphology of tin (001) epitaxial layers, *Physical Review B* 61 (2000) 16137.
- [15] K. Yokota, K. Nakamura, T. Kasuya, K. Mukai, M. Ohnishi, Resistivities of titanium nitride films prepared onto silicon by an ion beam assisted deposition method, *Journal of Physics D: Applied Physics* 37 (2004) 1095.
- [16] S. Zhang, F. Yan, Y. Yang, M. Yan, Y. Zhang, J. Guo, H. Li, Effects of sputtering gas on microstructure and tribological properties of titanium nitride films, *Applied Surface Science* 488 (2019) 61–69.
- [17] N. Sun, D. Zhou, S. Shi, F. Liu, W. Liu, Q. Chen, P. Zhao, S. Li, J. Wang, Superior-performance TiN films sputtered for capacitor electrodes, *Journal of Materials Science* 54 (2019) 10346–10354.
- [18] P. Patsalas, C. Charitidis, S. Logothetidis, The effect of substrate temperature and biasing on the mechanical properties and structure of sputtered titanium nitride thin films, *Surface and Coatings Technology* 125 (2000) 335–340.
- [19] C. H. Ma, J. H. Huang, H. Chen, Nanohardness of nanocrystalline TiN thin films, *Surface and Coatings Technology* 200 (2006) 3868–3875.

- [20] B. Kearney, B. Jugdersuren, J. Culbertson, P. Desario, X. Liu, Substrate and annealing temperature dependent electrical resistivity of sputtered titanium nitride thin films, *Thin Solid Films* 661 (2018) 78–83.
- [21] M. Jones, I. McColl, D. Grant, Effect of substrate preparation and deposition conditions on the preferred orientation of TiN coatings deposited by RF reactive sputtering, *Surface and Coatings Technology* 132 (2000) 143–151.
- [22] V. Matias, R. H. Hammond, Ion beam induced crystalline texturing during thin film deposition, *Surface and Coatings Technology* 264 (2015) 1–8.
- [23] H. Ljungcrantz, M. Odén, L. Hultman, J. Greene, J. E. Sundgren, Nanoindentation studies of single-crystal (001)-, (011)-, and (111)-oriented TiN layers on MgO, *Journal of Applied Physics* 80 (1996) 6725–6733.
- [24] G. Martinez, V. Shutthanandan, S. Thevuthasan, J. Chessa, C. Ramana, Effect of thickness on the structure, composition and properties of titanium nitride nano-coatings, *Ceramics International* 40 (2014) 5757–5764.
- [25] Z. He, S. Zhang, D. Sun, Effect of bias on structure mechanical properties and corrosion resistance of TiN_x films prepared by ion source assisted magnetron sputtering, *Thin Solid Films* 676 (2019) 60–67.
- [26] T. Kaizuka, H. Shinriki, N. Takeyasu, T. Ohta, Conformal chemical vapor deposition TiN (111) film formation as an underlayer of Al for highly reliable interconnects, *Japanese journal of applied physics* 33 (1994) 470.
- [27] W. Ensinger, Low energy ion assist during deposition an effective tool for controlling thin film microstructure, *Nuclear Instruments and Methods in Physics Research Section B: Beam Interactions with Materials and Atoms* 127 (1997) 796–808.
- [28] M. Lattemann, U. Helmersson, J. Greene, Fully dense, non-faceted 111-textured high power impulse magnetron sputtering tin films grown in the absence of substrate heating and bias, *Thin Solid Films* 518 (2010) 5978–5980.
- [29] F. Cemin, G. Abadias, T. Minea, D. Lundin, Tuning high power impulse magnetron sputtering discharge and substrate bias conditions to reduce the intrinsic stress of tin thin films, *Thin Solid Films* (2019).
- [30] G. Abadias, Y. Tse, P. Guérin, V. Pelosin, Interdependence between stress, preferred orientation, and surface morphology of nanocrystalline tin thin films deposited by dual ion beam sputtering, *Journal of applied physics* 99 (2006) 113519.
- [31] Z. Y. Yang, Y. H. Chen, B. H. Liao, K. P. Chen, Room temperature fabrication of titanium nitride thin films as plasmonic materials by high-power impulse magnetron sputtering, *Optical Materials Express* 6 (2016) 540–551.
- [32] V. Merie, M. Pustan, G. Negrea, C. Birleanu, Research on titanium nitride thin films deposited by reactive magnetron sputtering for mems applications, *Applied Surface Science* 358 (2015) 525–532.
- [33] P. Patsalas, S. Logothetidis, Optical, electronic, and transport properties of nanocrystalline titanium nitride thin films, *Journal of Applied Physics* 90 (2001) 4725–4734.
- [34] J.-S. Chun, I. Petrov, J. Greene, Dense fully 111-textured tin diffusion barriers: Enhanced lifetime through microstructure control during layer growth, *Journal of applied physics* 86 (1999) 3633–3641.
- [35] S. M. Amir, M. Gupta, A. Gupta, J. Stahn, A. Wildes, Surfactant induced symmetric and thermally stable interfaces in Cu/Co multilayers, *Journal of Physics: Condensed Matter* 23 (2011) 485003.

- [36] S. Chowdhury, R. Gupta, S. Prakash, L. Behera, D. M. Phase, M. Gupta, Supporting Material submitted along with this work. It provides information regarding (i) Schematic diagram of ion beam sputtering chamber
(ii) Detailed fitting parameters obtained from fitting of XRD data
(iii) Detailed values of N K-edge features
(iv) Detailed analysis of AFM data (2020).
- [37] D. M. Phase, M. Gupta, S. Potdar, L. Behera, R. Sah, A. Gupta, Development of soft X-ray polarized light beamline on Indus-2 synchrotron radiation source, *AIP Conference Proceedings* 1591 (2014) 685–686.
- [38] G. S. Henderson, F. M. De Groot, B. J. Moulton, X-ray absorption near-edge structure (XANES) spectroscopy, *Reviews in Mineralogy and Geochemistry* 78 (2014) 75–138.
- [39] J. F. Ziegler, M. D. Ziegler, J. P. Biersack, SRIM—the stopping and range of ions in matter (2010), *Nuclear Instruments and Methods in Physics Research Section B: Beam Interactions with Materials and Atoms* 268 (2010) 1818–1823.
- [40] C. Braun, Parratt 32 Program for Reflectivity Fitting, Hahn-Meitner Institute, Berlin (1999).
- [41] L. G. Parratt, Surface studies of solids by total reflection of X-rays, *Physical Review B* 95 (1954) 359–369.
- [42] M. Tolan, *X-Ray Scattering from Soft-Matter Thin Films: Materials Science and Basic Research*, volume 148, Springer, 1999.
- [43] A. Tiwari, M. Tiwari, M. Gupta, H. C. Wille, A. Gupta, Interface sharpening in miscible and isotopic multilayers: Role of short-circuit diffusion, *Physical Review B* 99 (2019) 205413.
- [44] S. Schiller, G. Beister, W. Sieber, Reactive high rate DC sputtering: Deposition rate, stoichiometry and features of TiO_x and TiN_x films with respect to the target mode, *Thin Solid Films* 111 (1984) 259 – 268.
- [45] S. Berg, T. Nyberg, Fundamental understanding and modeling of reactive sputtering processes, *Thin Solid Films* 476 (2005) 215 – 230.
- [46] A. Anders, Tutorial: Reactive high power impulse magnetron sputtering (R-HiPIMS), *Journal of Applied Physics* 121 (2017) 171101.
- [47] J. Stanislav, J. Sikac, M. Cermak, Properties of magnetron-deposited polycrystalline TiN layers, *Thin Solid Films* 191 (1990) 255–273.
- [48] J. E. Sundgren, B. O. Johansson, S. E. Karlsson, Mechanisms of reactive sputtering of titanium nitride and titanium carbide I: Influence of process parameters on film composition, *Thin Solid Films* 105 (1983) 353–366.
- [49] P. Patsalas, C. Gravalidis, S. Logothetidis, Surface kinetics and subplantation phenomena affecting the texture, morphology, stress, and growth evolution of titanium nitride films, *Journal of Applied Physics* 96 (2004) 6234–6246.
- [50] J. Pelleg, L. Zevin, S. Lungo, N. Croitoru, Reactive-sputter-deposited TiN films on glass substrates, *Thin Solid Films* 197 (1991) 117 – 128.
- [51] F. Esaka, K. Furuya, H. Shimada, M. Iamura, N. Matsubayashi, H. Sato, A. Nishijima, A. Kawana, H. Ichimura, T. Kikuchi, Comparison of surface oxidation of titanium nitride and chromium nitride films studied by X-ray absorption and photoelectron spectroscopy, *Journal of Vacuum Science & Technology A: Vacuum, Surfaces, and Films* 15 (1997) 2521–2528.
- [52] V. Valvoda, R. ern, R. Kuel, J. Musil, V. Poulek, Dependence of microstructure of TiN coatings on their thickness, *Thin Solid Films* 158 (1988) 225 – 232.
- [53] J. E. Sundgren, Structure and properties of TiN coatings, *Thin solid films* 128 (1985) 21–44.
- [54] F. Elstner, A. Ehrlich, H. Giegengack, H. Kupfer, F. Richter, Structure and properties of titanium nitride thin films deposited at low

- temperatures using direct current magnetron sputtering, *Journal of Vacuum Science & Technology A: Vacuum, Surfaces, and Films* 12 (1994) 476–483.
- [55] A. Gibaud, S. Hazra, X-ray reflectivity and diffuse scattering, *Current Science* (2000) 1467–1477.
- [56] S. Mahieu, D. Depla, Reactive sputter deposition of tin layers: modelling the growth by characterization of particle fluxes towards the substrate, *Journal of Physics D: Applied Physics* 42 (2009) 053002.
- [57] M. Gupta, S. Amir, A. Gupta, J. Stahn, Surfactant mediated growth of Ti/Ni multilayers, *Applied Physics Letters* 98 (2011) 101912.
- [58] M. Larsson, M. Bromark, P. Hedenqvist, S. Hogmark, Deposition and mechanical properties of multilayered PVD Ti- TiN coatings, *Surface and Coatings Technology* 76 (1995) 202–205.
- [59] M. Roy, N. R. Mucha, R. G. Ponnampaloor, P. Jaipan, O. Scott-Emuakpor, S. Yarmolenko, A. K. Majumdar, D. Kumar, Quantum interference effects in titanium nitride films at low temperatures, *Thin Solid Films* 681 (2019) 1–5.
- [60] R. Ningthoujam, N. Gajbhiye, Synthesis, electron transport properties of transition metal nitrides and applications, *Progress in Materials Science* 70 (2015) 50–154.
- [61] B. Ravel, M. Newville, ATHENA, ARTEMIS, HEPHAESTUS: data analysis for X-ray absorption spectroscopy using IFEFFIT, *Journal of Synchrotron Radiation* 12 (2005) 537–541.
- [62] P. Lazar, J. Redinger, J. Strobl, R. Podloucky, B. Rashkova, G. Dehm, G. Kothleitner, S. Šturm, K. Kutschej, C. Mitterer, et al., NK electron energy-loss near-edge structures for TiN/VN layers: an ab initio and experimental study, *Analytical and Bioanalytical Chemistry* 390 (2008) 1447–1453.
- [63] J. Pflüger, J. Fink, G. Crecelius, K. Bohnen, H. Winter, Electronic structure of unoccupied states of TiC, TiN, and VN by electron-energy-loss-spectroscopy, *Solid State Communications* 44 (1982) 489–492.
- [64] J. G. Chen, NEXAFS investigations of transition metal oxides, nitrides, carbides, sulfides and other interstitial compounds, *Surface Science Reports* 30 (1997) 1–152.
- [65] L. Soriano, M. Abbate, H. Pen, M. Czyżyk, J. Fuggle, The interaction of N with Ti and the oxidation of TiN studied by soft x-ray absorption spectroscopy, *Journal of Electron Spectroscopy and Related Phenomena* 62 (1993) 197–206.
- [66] R. Gupta, M. Gupta, D. Phase, Early stages of TiN thin film growth probed using in-situ soft X-ray absorption spectroscopy, in: *AIP Conference Proceedings*, volume 1832, 2017, p. 080081.
- [67] Y. Hu, T. Sham, Z. Zou, G. Xu, L. Chan, B. Yates, G. Bancroft, A study of titanium nitride diffusion barriers between aluminium and silicon by X-ray absorption spectroscopy: the Si, Ti and N results, *Journal of Synchrotron Radiation* 8 (2001) 860–862.
- [68] A. Niesen, M. Glas, J. Ludwig, J.-M. Schmalhorst, R. Sahoo, D. Ebke, E. Arenholz, G. Reiss, Titanium nitride as a seed layer for Heusler compounds, *Journal of Applied Physics* 118 (2015) 243904.